

Synthesis of Mn-based nanoparticles through polyol process under solvothermal conditions

E. Pantelidou¹, C. Dendrinou-Samara^{1}*

¹Laboratory of Inorganic Chemistry, Department of Chemistry, Aristotle University of Thessaloniki, 54124 Thessaloniki, Greece

* Corresponding author

Abstract

Manganese-based nanoparticles (NPs) constitute a versatile class of inorganic materials with significant potential in catalysis, energy storage, and biomedical applications. In this study, a systematic investigation into the polyol-mediated solvothermal synthesis of Mn-based NPs with diverse compositions—including MnCO_3 , MnOHCO_3 , and mixed-valence manganese oxides—is presented. Using polyols of distinct physicochemical properties (propylene glycol, PG, and tetraethylene glycol, TEG), various manganese precursors (KMnO_4 , $\text{MnCl}_2 \cdot 4\text{H}_2\text{O}$, $\text{Mn}(\text{acac})_2$, $\text{Mn}(\text{NO}_3)_2 \cdot x\text{H}_2\text{O}$), and both organic and inorganic reducing agents (oleylamine, OAm; NaOH), we elucidate the influence of precursor chemistry and reaction environment on nanoparticle formation. Structural, morphological, and compositional analyses (XRD, TEM/SEM-EDS, FTIR, TGA, DLS, and UV–Vis spectroscopy) reveal controlled synthesis of phase-pure MnCO_3 , MnOHCO_3 , and $\text{Mn}_2\text{O}_3/\text{MnO}_2$ nanoparticles with distinct nanostructures and organic surface coatings derived from polyol oxidation products. Notably, MnOHCO_3 nanoparticles are successfully synthesized for the first time, highlighting the crucial role of hydroxyl incorporation promoted by NaOH. The optical, colloidal, and thermochemical properties further underscore the suitability of these nanomaterials for semiconductive, catalytic, and biomedical applications. Overall, this work provides fundamental insights into the polyol solvothermal synthesis mechanism and introduces MnOHCO_3 as a new Mn-based nanomaterial with promising potential for future technological applications.

1. Introduction

Inorganic nanoparticles (NPs) have emerged as a remarkable class of materials with multifaceted applications in various scientific and technological fields, including catalysis, energy storage, and biomedical applications.¹⁻⁵ Among the transition metal NPs, manganese-based, most commonly manganese oxide (Mn_xO_y) and manganese carbonate ($MnCO_3$) NPs, exhibit exceptional potential due to their unique properties, such as high magnetic susceptibility, catalytic activity, biocompatibility and strong adsorption capacity. Therefore, the synthesis of these NPs has commanded substantial attention in recent research endeavors⁶⁻¹⁰.

Manganese oxide NPs are a versatile class of nanomaterials with a rich array of properties and applications, including materials science¹¹⁻¹³, environmental science¹⁴⁻¹⁶, and medicine^{8,17,18}. Their chemical composition consists of various forms, including MnO , Mn_2O_3 , Mn_3O_4 and MnO_2 , each offering distinct properties and reactivity^{19,20}. Notably, Mn_3O_4 exhibits ferromagnetic behavior or superparamagnetic behavior at the nanoscale^{21,22,23}, that can be exploited in applications like magnetic data storage²⁴ and targeted drug delivery²⁵. These NPs also showcase diverse electrical conductivity based on their crystal structure and oxidation state²⁶, with MnO_2 NPs being used in supercapacitors and batteries due to their high electrical conductivity^{11,27,28}. Moreover, they possess high catalytic activity in various chemical reactions^{8,29}, including oxidation and reduction processes^{30,31}, and high adsorption capacity^{32,33}. Their optical properties, including fluorescence and UV-visible absorption, are harnessed in sensing applications and in combination with their biocompatibility they can be used in potential applications in drug delivery and biomedical imaging³⁴⁻³⁶.

In general, most manganese oxides are self-therapeutic^{6,8}. Particularly, among the three oxidation states of manganese, Mn^{2+} ions show the best stability due to the semi-substituted outer 3d orbitals. As a result, Mn^{3+} and Mn^{4+} ions possess oxidation capacity and can react with intracellular reducing substances, such as GSH, whereby participating in redox reactions they are reduced to Mn^{2+} and glutathione is oxidized. This interaction of oxidative MnO_2 , Mn_2O_3 and Mn_3O_4 with cells leads to intracellular depletion of GSH, which further affects several complex biochemical reactions. At the same time, different valence states of manganese exhibit different magnetism, specifically low valence manganese ions exhibit better relaxivity r_1 due to more uncoupled electrons. Thus, Mn^{2+} ions show the strongest r_1 relaxivity and are ideal candidates for MRI^{8,37}.

Manganese carbonate ($MnCO_3$) is an environmentally friendly material that is found in abundance on earth and at the same time possesses low toxicity and high biocompatibility^{9,38}. In particular, the low

valence (+2) state of MnCO_3 facilitates the insertion/removal of hydroxyl ions to form MnOHCO_3 through electrochemical reaction, leading to manganese-rich valence states (Mn^{2+} , Mn^{3+} , Mn^{4+} , etc.). This property as well as high electrochemical active centers, rich Faradaic redox process and low cost make it a new emerging material for innumerable applications in the field of electrochemical devices and catalysts, such as electrodes for supercapacitors as well as batteries. The stabilization of the octahedral $[\text{MnO}_6]$ structure due to the carbonate planes in the structure of rhodochrosite can also be beneficial for the occurrence of electrochemical reactions mainly on the electrode surface and endow longer cyclic lifetime as a pseudocapacitor³⁸⁻⁴⁰. Moreover, MnCO_3 NPs can act as effective T_1 contrast agents in magnetic resonance imaging by producing Mn^{2+} ions, which are simultaneously sensitive to acidic conditions further increasing the sensitivity in diagnosis. In parallel, under ultrasound irradiation they can efficiently produce hydroxyl radicals ($\cdot\text{OH}$) and singlet oxygen ($^1\text{O}_2$) while releasing CO_2 and Mn^{2+} due to the degradation they undergo when in the local acidic tumor microenvironment. These properties make MnCO_3 NPs an attractive material for biological applications such as drug delivery and imaging⁴¹⁻⁴³. Lastly, MnCO_3 provides an important and powerful precursor for the synthesis of manganese oxides through high temperature calcination process^{9,38,40}.

Herein, we present a comprehensive investigation into the synthesis of Mn-based NPs with diverse compositions such as Mn_xO_y , MnCO_3 and MnOHCO_3 , utilizing the polyol process under solvothermal conditions. The synthesis method explored involves the reduction of manganese precursors in a polyol medium via solvothermal treatment at elevated temperatures. The polyol process is an effective method for producing NPs with precise control over size, shape, and composition and can also lead to the formation of biocompatible organic coatings. The mechanism of the polyol process comprises of redox, complexation and decomposition reactions with the cations and anions of the solution. The products of the redox reactions are oxidized derivatives of polyols, like glycolaldehyde, glyoxylic acid, glycolic acid, oxalic acid, oxalates and even CO_2 ⁴⁴⁻⁴⁶. Solvothermal conditions, involving a combination of high temperature and pressure, further enhance the versatility and efficiency of this synthetic approach, allowing for the synthesis of high-quality products⁴⁷. On that basis, glycols of different physicochemical properties such as 1,2-propylene glycol (PG) and tetraethylene glycol (TEG), manganese precursors of dissimilar redox potential and activity (KMnO_4 , $\text{Mn}(\text{acac})_2$, $\text{MnCl}_2 \cdot 4\text{H}_2\text{O}$ & $\text{Mn}(\text{NO}_3)_2 \cdot x\text{H}_2\text{O}$) and diverse type of reducing agents (organic, oleylamine (OAm) & inorganic, NaOH), have been employed. The resulting NPs will be characterized using a suite of advanced analytical techniques to assess their size, morphology, crystallinity, composition, and surface properties.

In general, this study aims to contribute to our understanding of the factors influencing the formation and properties of Mn-based NPs, which will be pivotal in tailoring their properties for specific applications. Also, the MnOHCO₃ NPs, which were successfully synthesized for the first time in our study, introduce a novel NP type that opens doors to transformative breakthroughs in diverse fields, from materials science to medicine.

2. Materials and methods

Chemicals and reagents: All the reagents were of analytical grade and were used directly without further purification: potassium permanganate (KMnO₄) (Aldrich, ≥ 99.9%, M = 158.03 g/mol), manganese (II) acetylacetone (Mn(acac)₂) (Aldrich, ≥ 99.9%, M = 253.15 g/mol), manganese (II) chloride tetrahydrate (MnCl₂·4H₂O) (Merc, ≥ 99.9%, M = 253.15 g/mol), manganese (II) nitrate hydrate (Mn(NO₃)₂·xH₂O) (Aldrich, ≥ 98%, M = 178.95 g/mol (anhydrous basis)), oleylamine (OAm) (J & K Scientific, ≥ 70%, M = 267.5 g/mol), 1,2-propylene glycol (PG) (Merck, ≥ 99%, M = 76.10 g/mol), tetraethylene glycol (TEG) (Merck, ≥ 99%, M = 194.23 g/mol), dimethyl sulfoxide (DMSO) (Aldrich, M = 78.13 g/mol)

2.1. Synthesis of Mn-based NPs

Sample **Mn1**: 0.2 g KMnO₄ (1.26 mmol) was dissolved in 8 mL of PG, and mixed well under stirring at 30 °C for 15 min. The supernatant was transferred into a Teflon-lined stainless-steel autoclave to set out a solvothermal polyol process. The reaction was carried out at 200 °C for 24 h, followed by natural cooling to room temperature. Afterward, the synthetic mixture was centrifuged at 5000 rpm for 20 min and washed three times with disolol, where the supernatants were discarded and a brown precipitate was acquired. The reaction yield was calculated at 5.45% based on the metal precursor.

Sample **Mn2**: 0.2 g MnCl₂·4H₂O (0.79 mmol) was dissolved in 2 mL of PG (solution 1). 2 mL of PG was mixed with 4 mL of OAm (solution 2). Both solutions were mixed well under stirring at 30 °C for 5 min. Afterwards the solution 2 was added to the solution 1 and was mixed well under stirring at 30 °C for another 10 min. The resulting solution was transferred into a Teflon-lined stainless-steel autoclave to set out a solvothermal polyol process. The reaction was carried out at 200 °C for 24 h, followed by natural cooling to room temperature. The reaction yield was calculated at 29.95% based on the metal precursor.

Sample Mn3: 0.2 g MnCl₂·4H₂O (0.79 mmol) was dissolved in 4 mL of PG. 0.2 g of NaOH was dissolved in 4 mL of PG (solution 2). Both solutions were mixed well under stirring at 30 °C for 5 min. Afterwards the solution 2 was added to the solution 1 and was mixed well under stirring at 30 °C for another 10 min. The resulting solution was transferred into a Teflon-lined stainless-steel autoclave to set out a solvothermal polyol process at 200 °C for 24 h. The reaction yield was calculated at 35.55% based on the metal precursor.

Sample Mn4: 0.2 g KMnO₄ (1.26 mmol) was dissolved in 8 mL of TEG, and mixed well under stirring at 30 °C for 15 min. The resulting solution was transferred into a Teflon-lined stainless-steel autoclave to set out a solvothermal polyol process at 200 °C for 24 h. The reaction yield was calculated at 58.25% based on the metal precursor.

Sample Mn5: 0.2 g Mn(acac)₂ (1.11 mmol) was dissolved in 4 mL of TEG. 0.2 g of NaOH was dissolved in 4 mL of TEG (solution 2). Both solutions were mixed well under stirring at 30 °C for 5 min. Afterwards the solution 2 was added to the solution 1 and was mixed well under stirring at 30 °C for another 10 min. The resulting solution was transferred into a Teflon-lined stainless-steel autoclave to set out a solvothermal polyol process at 200 °C for 24 h. The reaction yield was calculated at 30% based on the metal precursor.

Sample Mn6: 0.2 g Mn(NO₃)₂·xH₂O (1.12 mmol) was dissolved in 8 mL of TEG, and mixed well under stirring at 30 °C for 15 min. The resulting solution was transferred into a Teflon-lined stainless-steel autoclave to set out a solvothermal polyol process. The reaction was carried out at 200 °C for 24 h, followed by natural cooling to room temperature. The reaction yield was calculated at 23.9% based on the metal precursor.

It is important to highlight that the inclusion of an extra reducing agent was considered essential. This addition is crucial as, in its absence, the system results in the formation of soluble manganese compounds instead of nanoparticles. To elaborate, when 0.2 g of MnCl₂·4H₂O was combined with 8 mL of PG without the incorporation of a reducing agent, soluble compounds of manganese and PG were synthesized.

2.2. Characterization

The crystal structure and crystallite size of synthesized NPs were investigated through X-ray diffraction (XRD) ... performed in the 2θ region from 10 to 90° , with monochromatized Cu-Ka radiation ($\lambda = 1.5418 \text{ \AA}$). The chemical information of the NPs was determined by Fourier transform infrared spectroscopy (FT-IR) using Nicolet 6700 FT-IR spectrometer in the wavenumber range of $4000\text{-}400 \text{ cm}^{-1}$ (2 cm^{-1} resolutions; 30 scans). Transmission Electron Microscopy (TEM) images were obtained The morphology of the NPs was determined by a JEOL 840A scanning electron microscope (SEM) coupled with energy dispersive X-ray spectrometry (EDX) for estimating their elemental composition. Thermogravimetric analysis (TGA) was employed using SETA-RAM SetSys-1200 instrument and performed at a heating rate of $10 \text{ }^\circ\text{C}/\text{min}$ from room temperature to $900 \text{ }^\circ\text{C}$ under nitrogen atmosphere. UV/vis spectra were recorded with a Jasco V-750 double-beam UV/vis spectrophotometer. The hydrodynamic size and ζ -potential were measured using a Nano ZS Malvern apparatus at room temperature.

3. Results and Discussion

3.1. Mn-based NPs synthesized with PG

Figure 1 demonstrates the X-ray diffraction (XRD) graphs of the synthesized Mn-based NPs synthesized with PG. Starting with KMnO_4 precursor and in the presence of PG (Fig.1A) resulted in the formation of hexagonal MnCO_3 NPs with space group R-3c, as indicated by the diffraction peaks that correspond to the (012), (104), (006), (113), (202), (018) and (116) planes of MnCO_3 rhodochrosite phase (JCPDS no. 86-0172)⁴⁰. Lattice parameters were estimated at $a = b = 4.773 \text{ \AA}$, $c = 15.642 \text{ \AA}$, $\alpha = \beta = 90^\circ$, $\gamma = 120^\circ$ ^{48,49}. The absence of any additional peaks in the diffraction pattern serves as confirmation of the high purity of the manganese carbonate (MnCO_3) crystallite.

In the case of $\text{MnCl}_2 \cdot 4\text{H}_2\text{O}$ precursor and in the presence of PG (Fig.1A, B), both reducing agents employed resulted also in the synthesis of hexagonal MnCO_3 NPs as shown by the diffraction peaks that correspond to the (012), (104), (006), (110), (113), (202), (024), (018) and (116) planes of MnCO_3 rhodochrosite phase (JCPDS no. 86-0172). Lattice parameters were estimated at $a = b = 4.773 \text{ \AA}$, $c = 15.642 \text{ \AA}$, $\alpha = \beta = 90^\circ$, $\gamma = 120^\circ$.

The crystallite size of all phases was calculated from the Scherrer equation, $D = 0.891\lambda/\beta \cos\theta$, and the full width at half-maximum of the main peak of each crystallite phase. For the MnCO_3 phase of Mn1 the crystallite size is 26 nm, for Mn2 is 48 nm and for Mn3 is 38 nm, respectively.

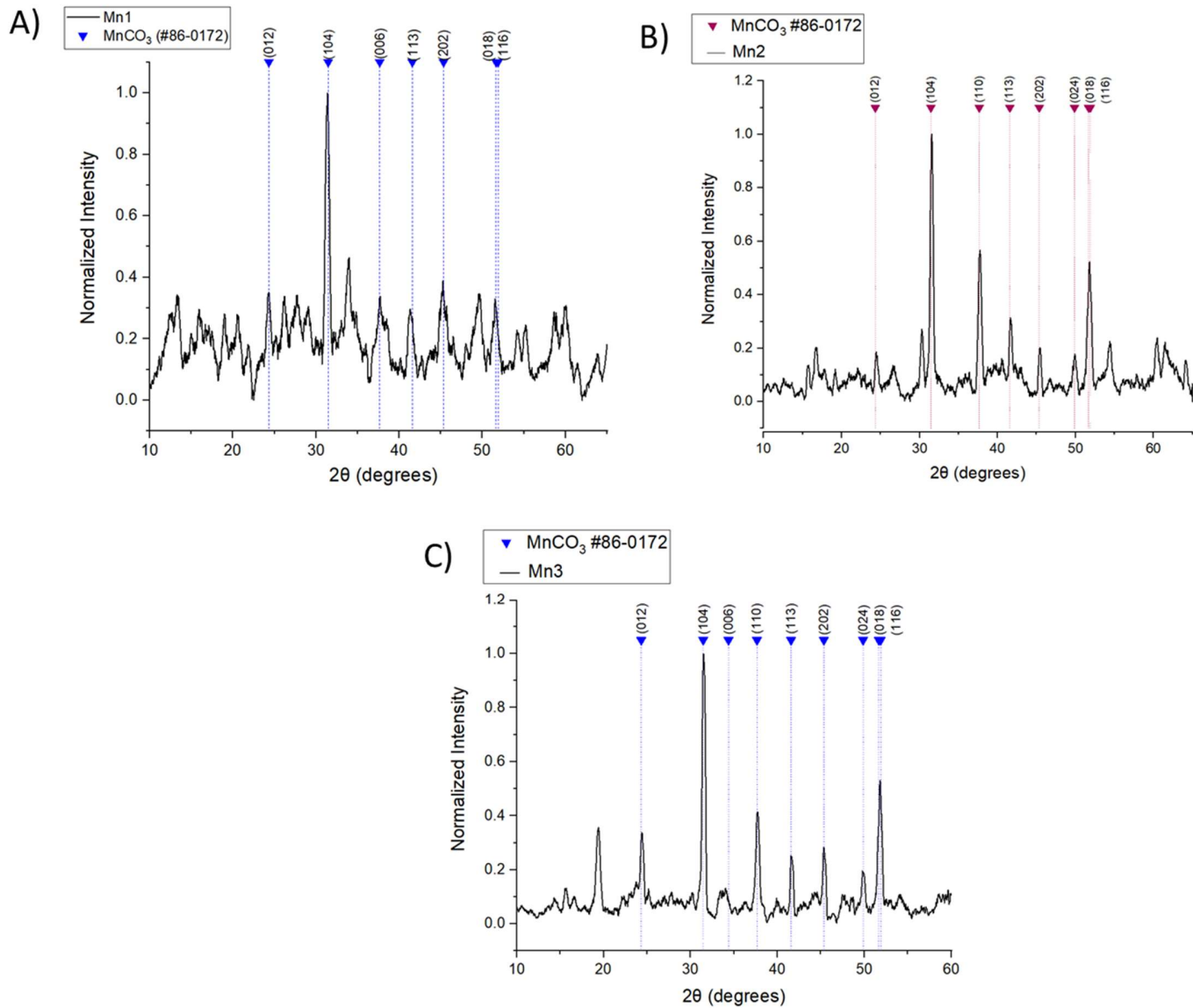


Figure 1. X-ray diffraction graphs of Mn-based NPs (Mn1, Mn2, Mn3) synthesized with PG.

The morphology of the synthesized NPs was investigated with electron microscopy. TEM images are presented in **Figure 2**. The Mn2 NPs (Fig. 2) have a mainly cubic or hexagonal shape with varying size distribution, with a maximum size of 140 nm.

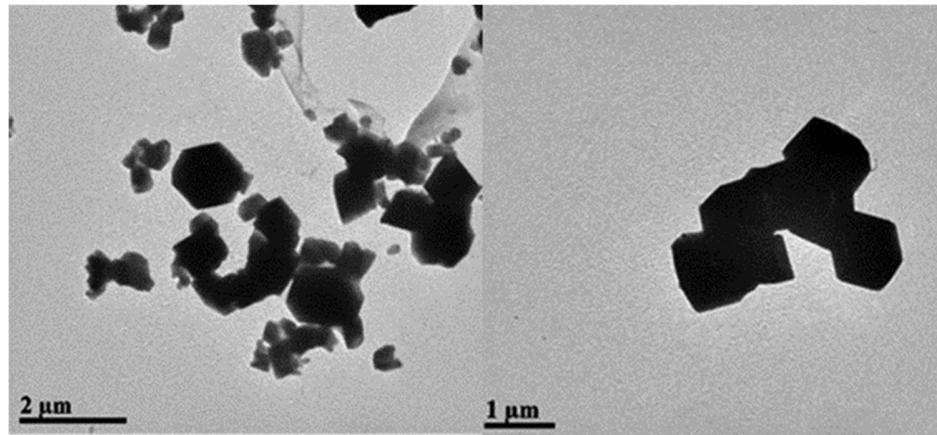
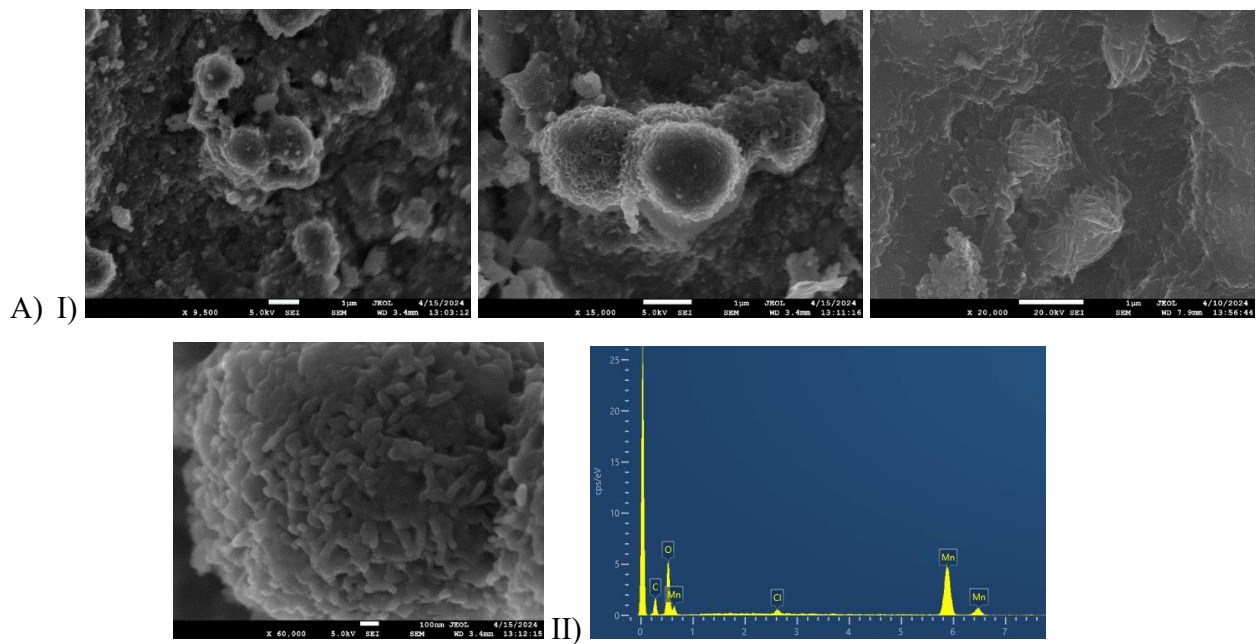
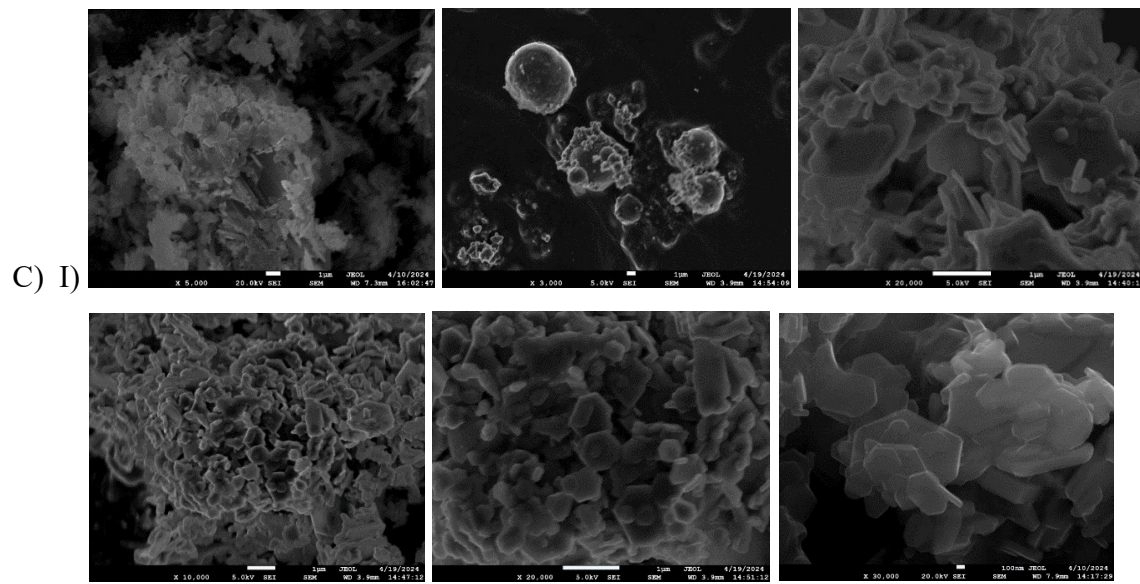
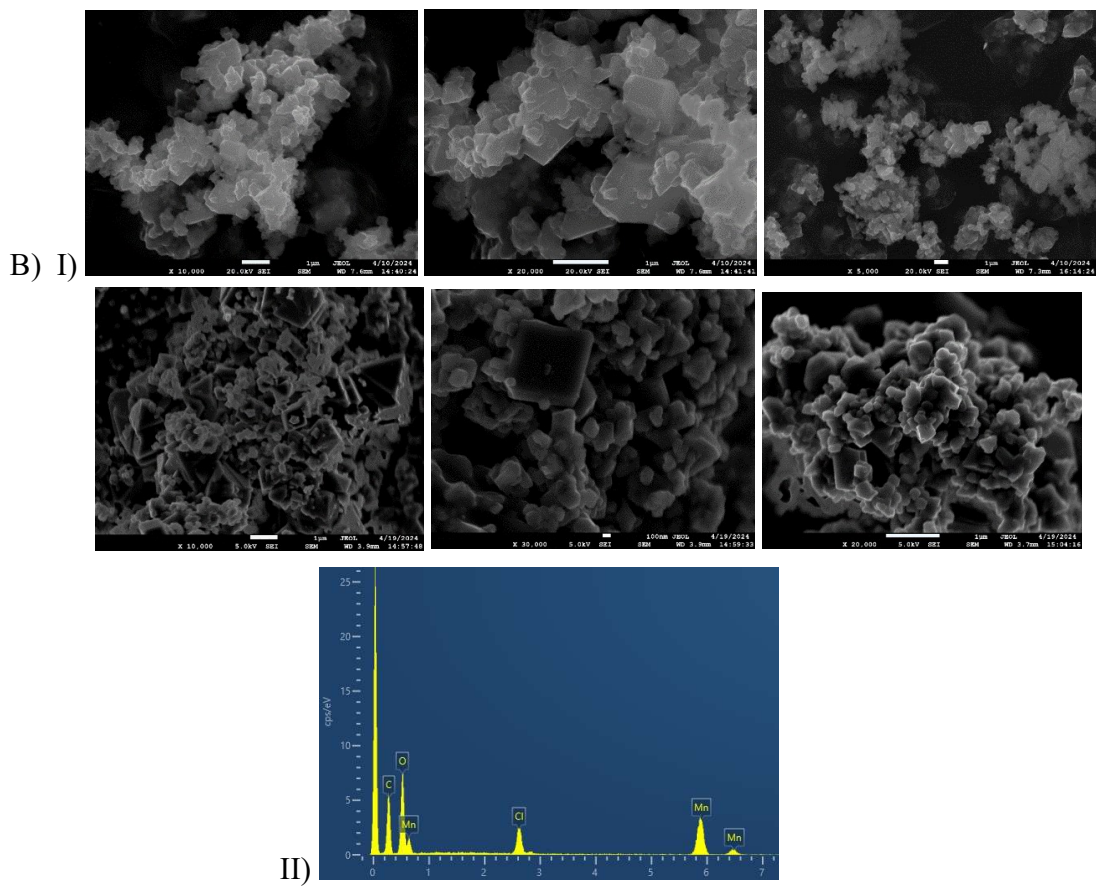


Figure 2. TEM images of Mn2 NPs.

Figure 3 demonstrates that Mn1 NPs possess a spherical morphology. For Mn2 Fig. 3B certifies their cubic or hexagonal shape of variable sizes. Mn3 NPs have the morphology of hexagonal nanoplates with a broad size distribution. The energy-dispersive X-ray spectroscopy (EDS) analysis results, which reveal the presence of carbon (C) and manganese (Mn) elements, are depicted in Fig. 3(II).





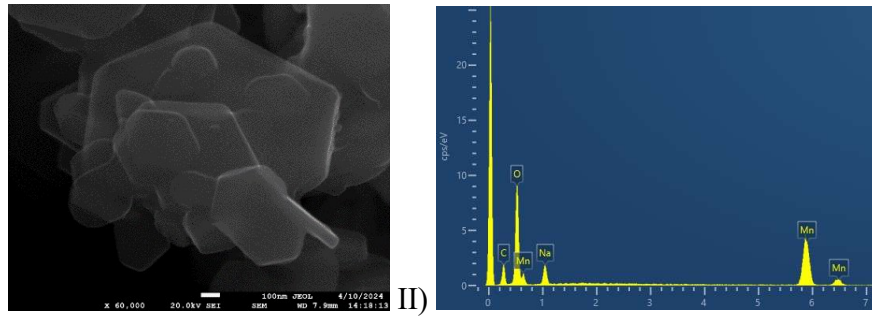


Figure 3. (I) SEM images of A) Mn1, B) Mn2, C) Mn3 NPs. (II) EDS spectra of A) Mn1, B) Mn2, C) Mn3.

The presence of the organic coating on the surface of the NPs has been confirmed by FTIR spectra (**Figure 4**). In the FT-IR spectrum of the Mn1 (Fig. 4A), the absorptions at 2981 and 2928 cm^{-1} are attributed to the bending vibrations of methylene groups -CH, -CH₂-, -CH₃, derived from propylene glycol. The characteristic peaks at 1421, 860 and 722 cm^{-1} are attributed to the vibrations of CO₃ groups⁴³. The absorption at 641 cm^{-1} is attributed to the lattice vibrations of Mn–O bond⁹. In the spectrum of the Mn2 (Fig. 4B), the strong absorptions at 3579 cm^{-1} and 3561 cm^{-1} are attributed to the N-H₂ bond, which confirms the existence of OAm on the surface of the NPs. Also, the absorptions at 2919 and 2852 cm^{-1} are attributed to the bending vibrations of the methylene groups -C-H, -CH₂-, -CH₃, which are derived from OAm^{50,51}. The peaks at 1404, 860 and 725 cm^{-1} are characteristic of the CO₃ groups and the absorptions at 666 and 622 cm^{-1} are attributed to the lattice vibrations of Mn–O bond. In the Mn3 spectrum (Fig. 4C) the characteristic peaks of the methylene groups vibrations, 2971 cm^{-1} , and the peaks at 1734 cm^{-1} and 1386 cm^{-1} suggest the presence of the oxidation derivatives of PG on the surface of NPs. There are also evident the characteristic absorptions of the CO₃ groups at 1404, 857 and 725 cm^{-1} and of the Mn-O bond at 457 and 417 cm^{-1} . The strong absorption at 3626 cm^{-1} is allotted to the presence of hydroxyl anions and in combination to the lower intensity of the peak at 1404 cm^{-1} suggest the adsorption of hydroxyl ions on the crystal lattice of MnCO₃ and consequently the formation of MnOHCO₃.

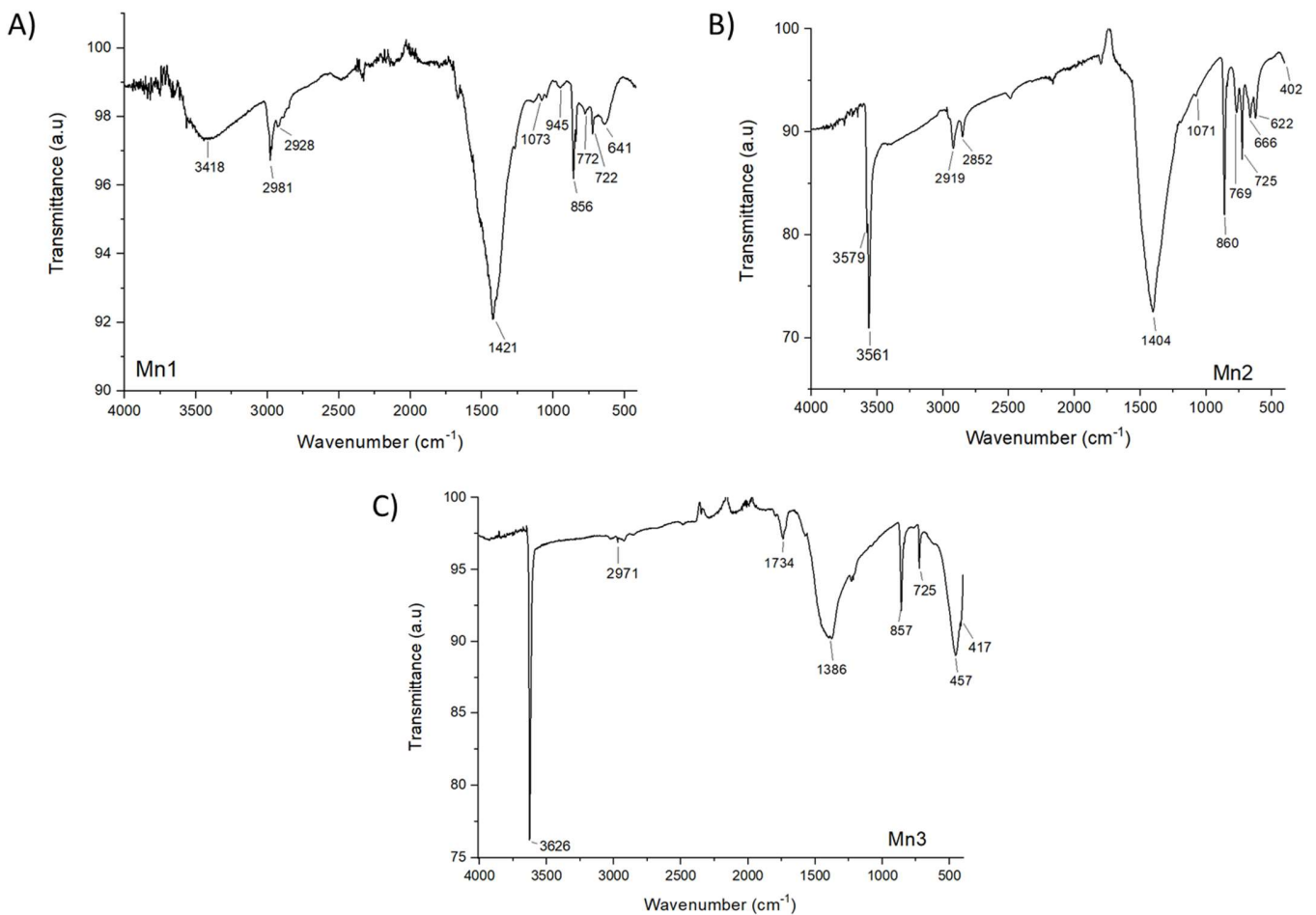
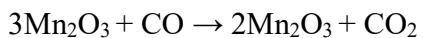
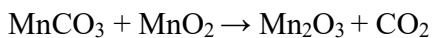
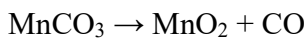


Figure 4. IR spectra of Mn-based NPs (Mn1, Mn2, Mn3) synthesized with PG.

Figure 5 shows the thermogravimetric curves of the NPs, presenting the weight loss in correlation to the temperature (25-900 °C). To investigate the percentage of carbon dioxide yielded by manganese carbonate, thermogravimetric analysis of bulk $\text{MnCO}_3 \cdot x\text{H}_2\text{O}$ (Fig. 5A) (MB 114.95 g/mol, moisture content 43-46%) was performed. In general, manganese carbonate undergoes thermal decomposition when heated in a nitrogen atmosphere, yielding CO_2 and MnO_2 which is simultaneously converted to Mn_2O_3 . Mn_2O_3 remains thermally stable up to 900°C and then decomposes to form $\text{Mn}_3\text{O}_4^{52}$.



In Figure 5A, from 20 to 155 °C, a weight loss of 2.5% is observed due to the removal of the moisture in the sample. From 155 to 491 °C, a sharp weigh loss of 32% is observed because of the manganese

carbonate which yields carbon dioxide (CO_2) and forms manganese oxides, where an increase in mass is observed, an exothermic effect, due to the oxidation of Mn_2O_3 and MnO_2 to Mn_3O_4 .

Initially, in the TGA curve of the MnCO_3 NPs (Fig. 5B) a 4% weight loss is observed from 20 to 80 °C, due to the removal of adsorbed water in the sample. As the temperature increases, from 80 to 400 °C, there is a sharp weight loss of 34% due to the decomposition of a quantity of organic compounds as well as the decomposition of manganese carbonate which gives off carbon dioxide (CO_2) and forms manganese oxides. The total weight loss of the NPs reaches 38% of its initial mass. Compared with the TGA curve of bulk MnCO_3 , it can be concluded that most of the weight loss comes from the decomposition of carbonate ions and a small percentage comes from the presence of organic compounds on the surface of MnCO_3 NPs. Also due to the nanoscale, the removal of organic compounds starts at lower temperatures and is finally completed at 400 °C compared to 500 °C of bulk MnCO_3 . For the MnCO_3 NPs with the OAm coating (Fig. 5C) an initial weight loss of 3% is evident, due to the removal of adsorbed water. As the heating continues, from 250 to 400°C, a sharp weight loss of 36% is recorded due to the decomposition of an amount of surfactant, oleylamine, which decomposes at 370 °C in nitrogen atmosphere⁵³, as well as the decomposition of part of manganese carbonate. The total weight loss of the NPs reaches 39% of its original mass. Compared with the TGA curve of bulk MnCO_3 , it can be concluded that the surfactant content is about 4% and the remaining percentage comes from the decomposition of carbonate ions. In the TGA curve of the MnOHCO_3 NPs (Fig. 5D), an initial weight loss of 2% from 20 to 102 °C is observed, due to moisture in the sample. Thereafter, a gradual removal of organics is observed, from 100 to 250 °C there is a weight loss of 9% and from 250 to 710 °C a weight loss of 8% due to the decomposition of low molecular weight organics, hydroxyls and the release of carbon dioxide. The total weight loss of the NPs reaches 19% of its initial mass.

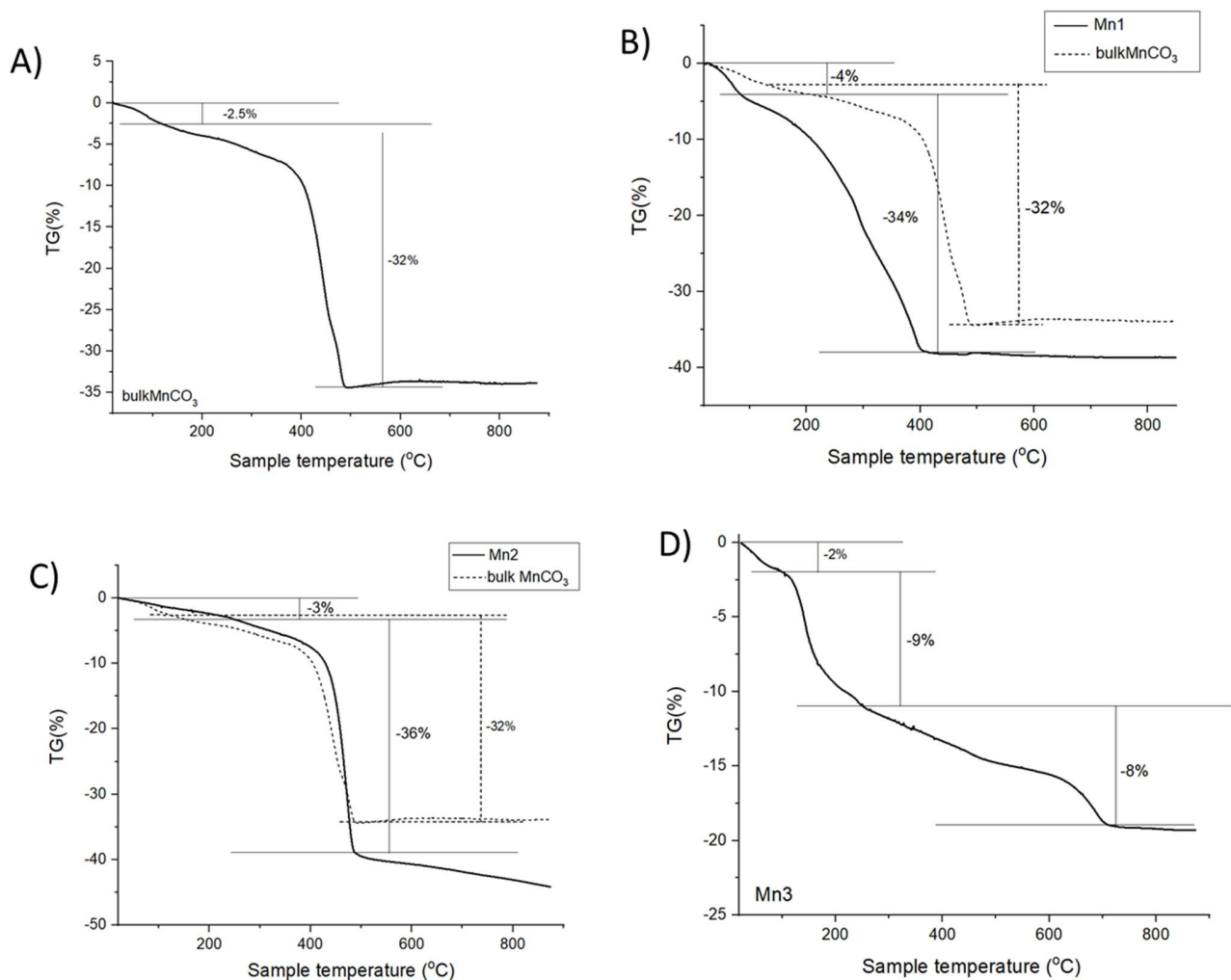
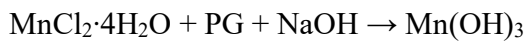
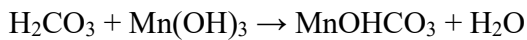


Figure 5. Thermogravimetric analysis (TGA) of Mn-based NPs (Mn1, Mn2, Mn3) synthesized with PG.

The structural composition and crystallite size of all synthesized NPs using PG are presented in **Table 1**. In the case of using PG and manganese source KMnO_4 the system is driven to produce NPs of pure MnCO_3 . This phenomenon arises because of the complete redox reaction that takes place, wherein Mn undergoes reduction from the +7 oxidation state to +2, while at the same time PG is completely oxidized to carbonate ions and a minor fraction remains in lower oxidation products.

The employment of $\text{MnCl}_2 \cdot 4\text{H}_2\text{O}$ as a manganese precursor, in conjunction with PG and the organic reducing agent OAm, results in coated MnCO_3 NPs. In contrast, utilizing the inorganic reducing agent NaOH, results in the synthesis of MnCO_3 NPs with hydroxyls in the crystal lattice, denoted as Mn(OHCO_3 . The underlying chemical reactions are articulated as follows:





Where Mn(OH)₃ is formed as an intermediate which promotes the formation of MnOHCO₃.

Table 1. Characterization of synthesized Mn-based NPs using PG.

Sample name	Precursor	Polyol	Reducing agent	Composition	dxRD (nm)	Org. coating (% w/w)	Carbonate ions (%w/w)
Mn1	KMnO ₄	PG	-	MnCO ₃	26	2	32
Mn2	MnCl ₂ ·4H ₂ O	PG	OAm	MnCO ₃	48	4	32
Mn3	MnCl ₂ ·4H ₂ O	PG	NaOH	MnOHCO ₃	38		

3.2. Mn-based NPs synthesized with TEG

Figure 6 demonstrates the X-ray diffraction (XRD) graphs of the synthesized Mn-based NPs synthesized with TEG. KMnO₄ precursor and in the presence of TEG (Fig.6A) resulted in the synthesis of hexagonal MnCO₃ NPs as shown from the diffraction peaks that correspond to the (012), (104), (006), (113), (202), (018) and (116) planes of MnCO₃ rhodochrosite phase (JCPDS no. 86-0172). Lattice parameters were estimated at $a = b = 4.773 \text{ \AA}$, $c = 15.642 \text{ \AA}$, $\alpha = \beta = 90^\circ$, $\gamma = 120^\circ$.

When using Mn(acac)₂ precursor in the presence of TEG and NaOH as a reducing agent (Fig.6B) resulted in the formation of hexagonal MnCO₃ NPs as displayed by the diffraction peaks that correspond to the (012), (104), (110), (113), (202), (024), (018) and (116) planes of MnCO₃ rhodochrosite phase (JCPDS no. 86-0172). Lattice parameters were estimated at $a = b = 4.773 \text{ \AA}$, $c = 15.642 \text{ \AA}$, $\alpha = \beta = 90^\circ$, $\gamma = 120^\circ$. In contrast, Mn(NO₃)₂·xH₂O in the presence of TEG (Fig.6C) lead to the synthesis of cubic phase bixbyite with space group Ia-3, Mn₂O₃ NPs (92%) with traces of cubic phase pyrolusite, MnO₂ (8%) as indicated by the diffraction peaks that correspond to the (211), (220), (222), (400), (420), (332), (431), (440), (433), (611), (620), (541), (622), (631) and (444) planes of Mn₂O₃ bixbyite phase (JCPDS no. 71-0636) and (110), (101), (200), (111), (210), (211), (220), (002), (310) and (221) planes of MnO₂ pyrolusite phase (JCPDS no. 81-2261). Lattice parameters were estimated at $a = b = c = 9.4146 \text{ \AA}$, $\alpha = \beta = \gamma = 90^\circ$ for Mn₂O₃⁵⁴, and $a = b = 4.4041 \text{ \AA}$, $c = 2.8765 \text{ \AA}$, $\alpha = \beta = \gamma = 90^\circ$ for MnO₂⁵⁵.

The crystallite size of Mn4 NPs was calculated 25 nm, of Mn5 41 nm and of the mixture Mn₂O₃/MnO₂, Mn6 NPs, 140 nm, respectively.

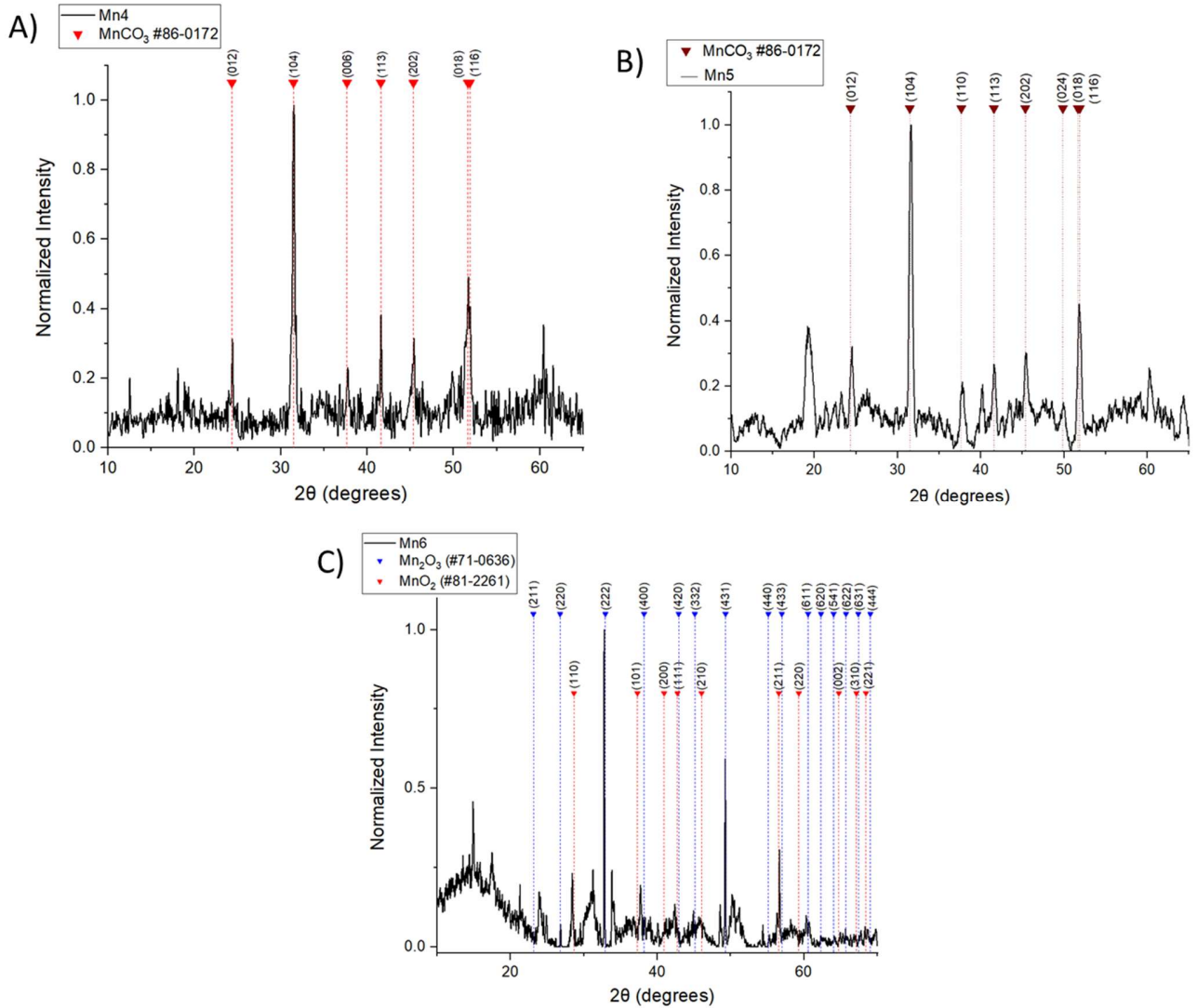


Figure 6. X-ray diffraction graphs of Mn-based NPs (Mn4, Mn5, Mn6) synthesized with TEG.

TEM images are presented in **Figure 7**. The Mn4 NPs (Fig. 7A) are located in clusters, which consist of rhombic-shaped nanoplates that form peanut-shaped aggregates with spiky edges. The Mn5 NPs (Fig. 7B) are in the form of clustered nanorods of varying size and roughness. Lastly, the Mn6 NPs (Fig. 7C) have no distinct shape and appear to have small size with irregular shape.

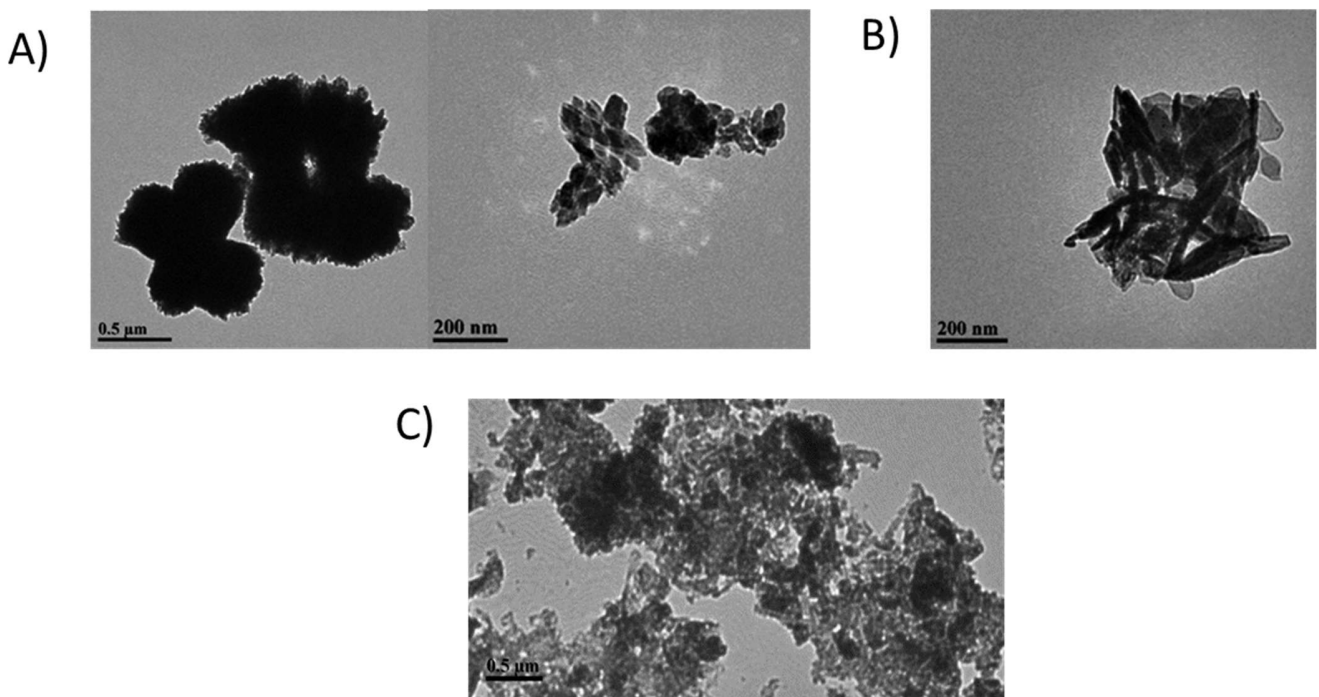
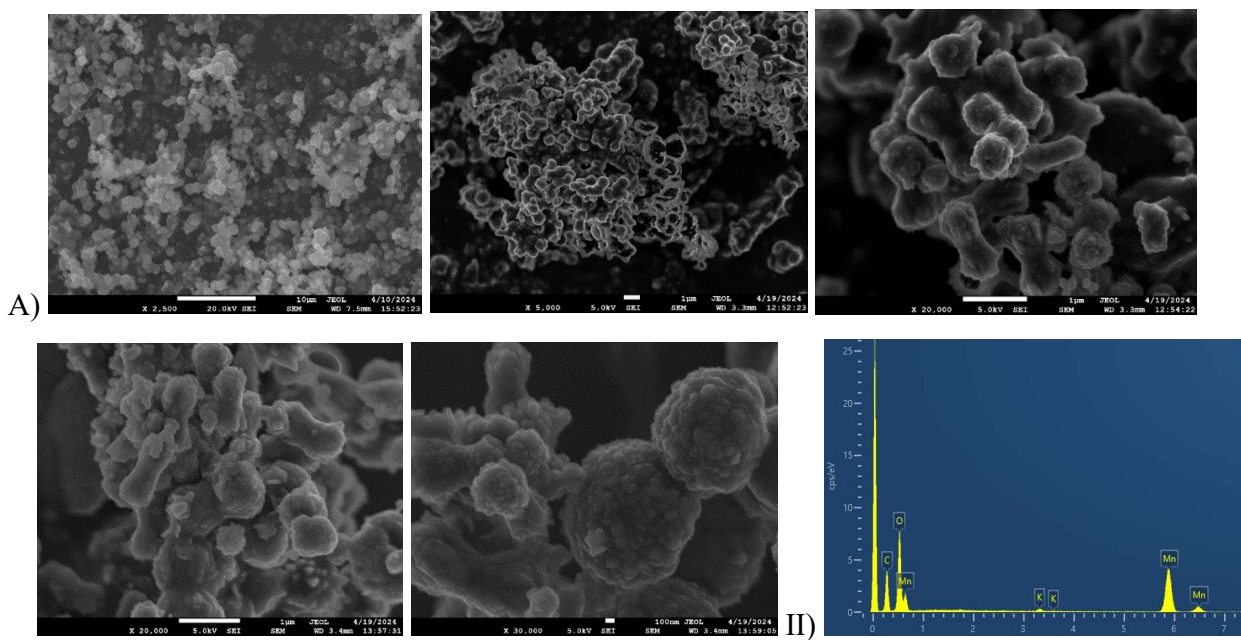
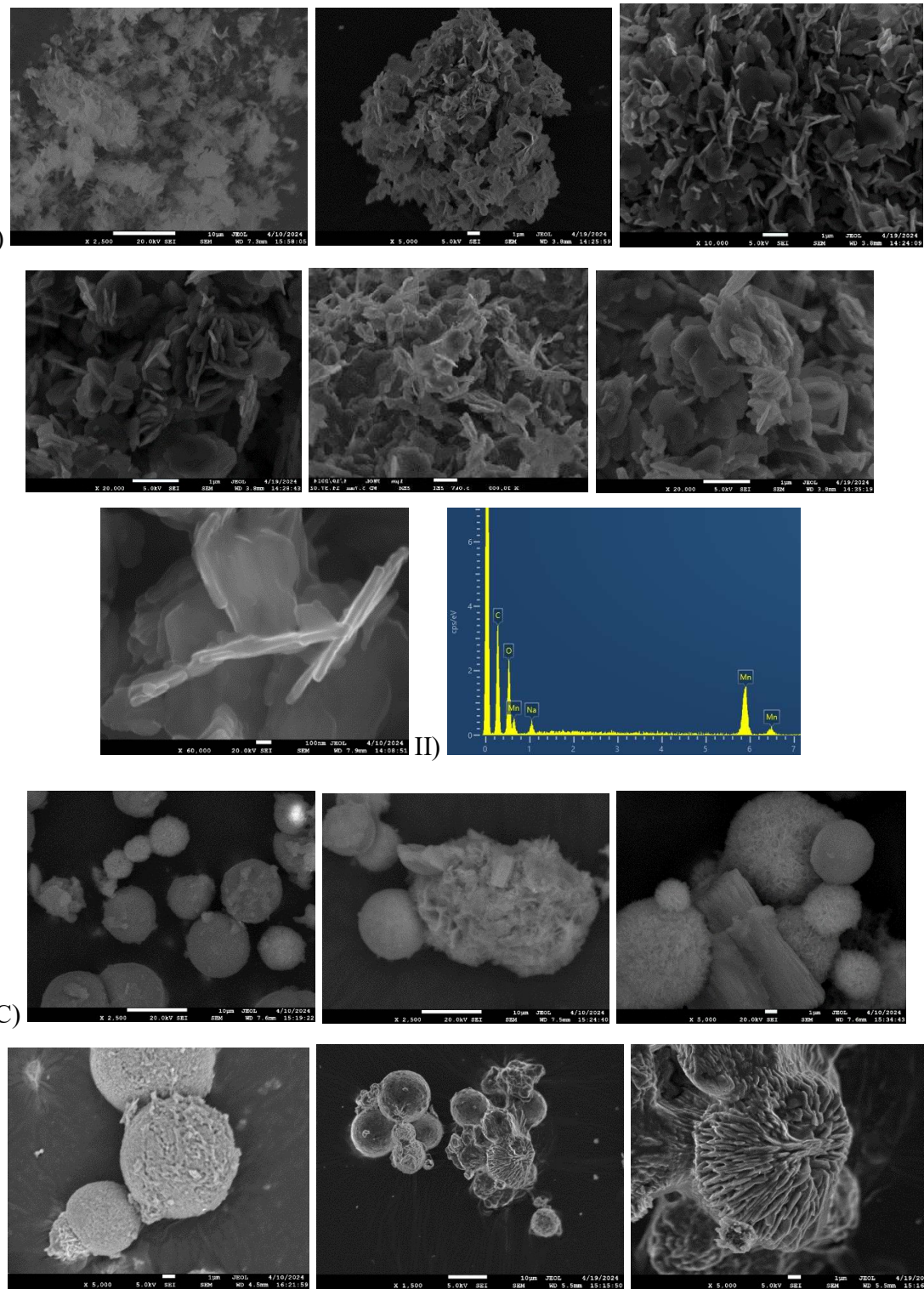


Figure 7. TEM images of Mn-based NPs (Mn4, Mn5, Mn6) synthesized with TEG.

Figure 8 displays the peanut-shaped aggregates with irregular edges formed by Mn4 nanoparticles (NPs), while Fig. 8B shows the nanorod aggregates formed by Mn5. Mn6 NPs exhibit a spherical morphology, as shown in Fig. 8C. The energy-dispersive X-ray spectroscopy (EDS) analysis results, indicating the presence of carbon (C) and manganese (Mn) elements, are presented in Fig. 8(II).





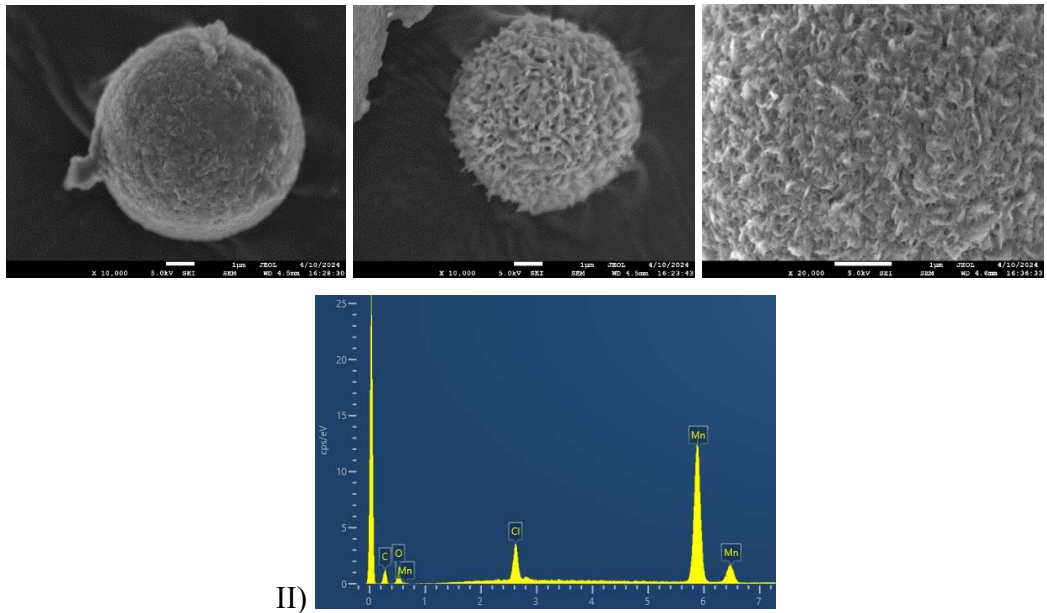


Figure 8. (I) SEM images of A) Mn4, B) Mn5, C) Mn6 NPs. (II) EDS spectra of A) Mn4, B) Mn5, C) Mn6.

Figure 9 presents the FTIR spectra of the synthesized NPs in the presence of TEG. In the Mn4 spectrum (Fig. 9A) the absorptions at 2980 and 2873 cm⁻¹ are attributed to the methylene groups vibrations. The peak at 1585 cm⁻¹, which corresponds to the vibrations of the C=O bond⁵⁶, and the multiplicity of the peak at 1403 cm⁻¹ certify the presence of the oxidation derivatives of TEG on the surface of NPs. Moreover, the characteristic absorptions of the CO₃ groups at 1403, 860 and 724 cm⁻¹ and of the Mn-O bond at 632 and 518 cm⁻¹ are apparent. In the Mn5 spectrum (Fig. 9B) the strong peak at 3625 cm⁻¹ indicates the presence of hydroxyl anions and in combination to the presence of the characteristic absorptions of the CO₃ groups at 1457, 877 and 713 cm⁻¹ verify the formation of MnOHCO₃. The peaks at 2921 and 2851 cm⁻¹ of the methylene groups vibrations and the peak at 1631 cm⁻¹ are attributed to the presence of the oxidation derivatives of TEG on the surface of NPs. Lastly, in the Mn6 spectrum (Fig. 9C) the broad band at 3460 cm⁻¹ is attributed to adsorbed water molecules. The peaks at 1118 and 1062 cm⁻¹ correspond to the C-O-C vibration and the absorptions at 861 and 759 cm⁻¹ are attributed to the in-plane C-H bond bending vibration, which are derived from TEG oxidation derivatives. The N-O bond stretching vibrations occur at 1575 and 1512 cm⁻¹ for the asymmetric N-O stretch and at 1397 and 1301 cm⁻¹ for the symmetric N-O stretch. The absorption at 504 cm⁻¹ is attributed to the vibrations of Mn–O bond.

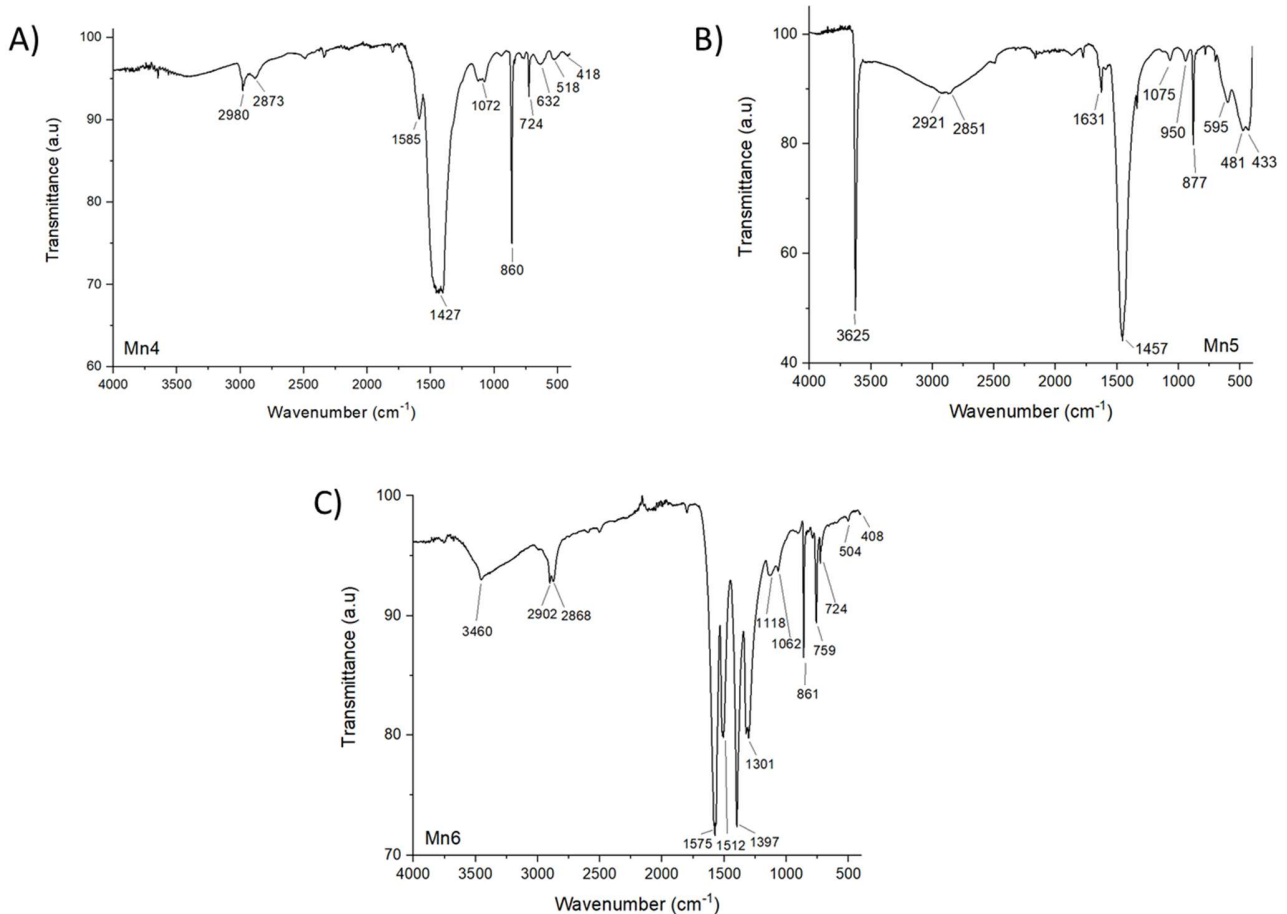


Figure 9. IR spectra of Mn-based NPs (Mn4, Mn5, Mn6) synthesized with TEG.

Figure 10 shows the TG curves of the NPs, presenting the weight loss in correlation to the temperature (25-900 °C). For the MnCO₃ NPs with the coating of TEG (Fig. 10A) a weight loss of 4% from 20 to 150 °C is obtained, due to water removal. As the heating continues, from 200 to 420 °C, a sharp weight loss of 34% is observed due to the decomposition of a quantity of the coating agent as well as the decomposition of manganese carbonate which gives off CO₂ and forms manganese oxides. The cumulative organic content (% w/w) is 38%. Compared with the TGA curve of bulk MnCO₃, it can be concluded that most of the weight loss comes from the decomposition of carbonate ions and a small percentage comes from the presence of organic compounds on the surface of MnCO₃ NPs. For the MnOHCO₃ NPs with the TEG coating (Fig. 10B) an initial weight loss of 3% from 20 to 125 °C is observed, due to moisture in the sample. Then the removal of organics takes place in two steps, from 125 to 210 °C there is a weight loss of 5% and from 210 to 412 °C a sudden weight loss of 15% due to the decomposition of low molecular weight organic compounds, hydroxyls and the release of carbon dioxide.

The total weight loss of the NPs reaches 23% of its original mass. Lastly, for the $\text{Mn}_2\text{O}_3/\text{MnO}_2$ NPs (Fig. 10C) the percentage of the moisture is 2%. From 100 to 440°C a sharp weight loss of 41% is observed due to the decomposition of TEG. The increase in mass, an exothermic effect, is due to the oxidation of Mn_2O_3 and MnO_2 to Mn_3O_4 . The cumulative organic content is 43%.

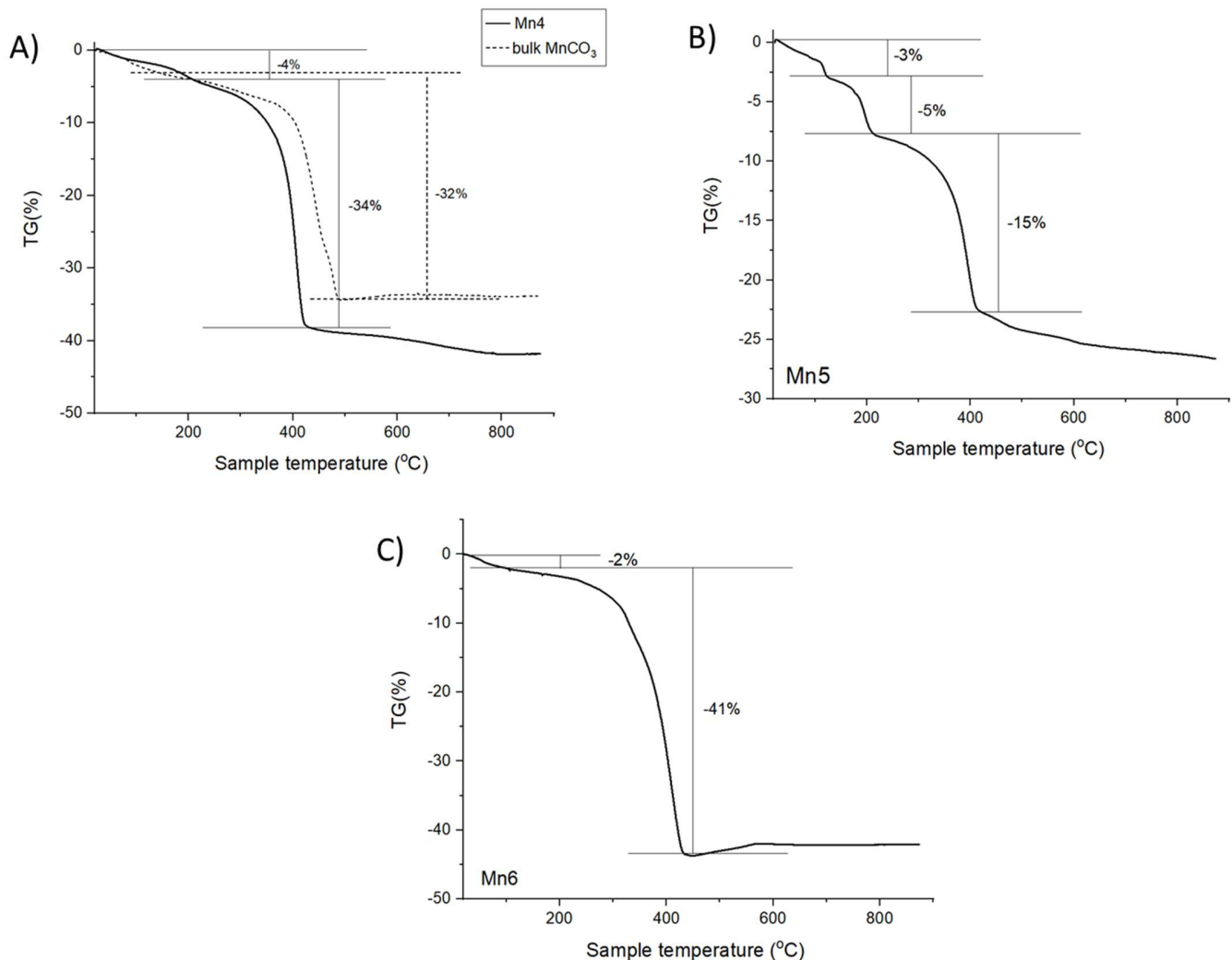


Figure 10. Thermogravimetric analysis (TGA) of Mn-based NPs (Mn4, Mn5, Mn6) synthesized with TEG.

The structural composition and crystallite size of all synthesized NPs using TEG as a polyol are presented in **Table 2**.

When employing KMnO_4 as the manganese source in the presence of TEG the system is directed towards the synthesis of pure MnCO_3 NPs. This outcome arises from a comprehensive redox reaction, where

manganese undergoes reduction from the +7 to +2. Concurrently, TEG undergoes complete oxidation, resulting in the formation of carbonate ions. Additionally, a small portion remains in lower oxidation products, such as ketones or aldehydes, serving as an organic coating on the surface of NPs.

In the case of the coordination Mn complex, $\text{Mn}(\text{acac})_2$, as a precursor and the use of an inorganic reducing agent, the synthesis of MnCO_3 NPs with hydroxyls in the crystal lattice, MnOHCO_3 NPs, takes place. This fact underscores that the utilization of NaOH induces the synthesis of MnOHCO_3 NPs.

Finally, in the context of employing $\text{Mn}(\text{NO}_3)_2 \cdot x\text{H}_2\text{O}$ as the manganese source in conjunction with TEG, the synthesis yields manganese oxide NPs. Specifically, a mixture of trivalent and tetravalent manganese oxide NPs is generated. This outcome is attributed to the competitive interaction between nitrate ions, serving as oxidizing agents, and the polyol's reducing function. Consequently, the polyol undergoes incomplete oxidation, with CO_2 not being fully produced as a result.

Table 2. Characterization of synthesized Mn-Based NPs using TEG.

Sample name	Precursor	Polyol	Reducing agent	Composition	dXRD (nm)	Org. coating (% w/w)	Carbonate ions (%w/w)
Mn4	KMnO_4	TEG	-	MnCO_3	25	2	32
Mn5	$\text{Mn}(\text{acac})_2$	TEG	NaOH	MnOHCO_3	41		
Mn6	$\text{Mn}(\text{NO}_3)_2 \cdot x\text{H}_2\text{O}$	TEG	-	Mn_2O_3 (92%) MnO_2 (8%)	140	41	-

The stabilization of synthesized Mn-based NPs was confirmed by measuring their average hydrodynamic particle size (Mean \pm PDI) and ζ -potential. The average size of $\text{MnCO}_3@\text{OAm}$ NPs is 293 ± 0.1 nm, while the ζ -potential was determined to be slightly positive $+8.7 \pm 1$ mV. In contrast, $\text{MnCO}_3@\text{TEG}$ NPs display a larger average size of 920 ± 0.213 nm, accompanied by an average ζ -potential of $+9.7 \pm 1.1$ mV. The increased hydrodynamic size can be attributed to particle aggregation, as corroborated by TEM images showcasing peanut-shaped structures. The $\text{MnOHCO}_3@\text{TEG}$ NPs have an average size of 1.31 ± 0.123 μm , with an average value of ζ -potential $+2.5 \pm 0.9$ mV, similarly indicating aggregation contributing to the larger hydrodynamic size. Finally, $\text{Mn}_2\text{O}_3/\text{MnO}_2@\text{TEG}$ NPs possess an average size of 322 ± 0.29 nm with a slightly negative value of ζ -potential -4.6 ± 1.3 mV.

The UV-Vis absorption spectrum analysis of MnCO_3 and MnOHCO_3 NPs reveals a broad absorption range spanning from 200 to 900 nm⁴³. Using Tauc's formula, the calculated band gaps for these NPs were found to be 2.3 eV for $\text{MnCO}_3@\text{OAm}$ NPs, 1.3 eV for $\text{MnCO}_3@\text{TEG}$ NPs, and 0.9 eV for

$\text{MnOHCO}_3@\text{TEG}$ NPs. This data underscores their suitability for semiconductive applications. In contrast, $\text{Mn}_2\text{O}_3/\text{MnO}_2@\text{TEG}$ NPs do not exhibit any UV-Vis absorption, and the band gap was determined to be 3.9 eV.

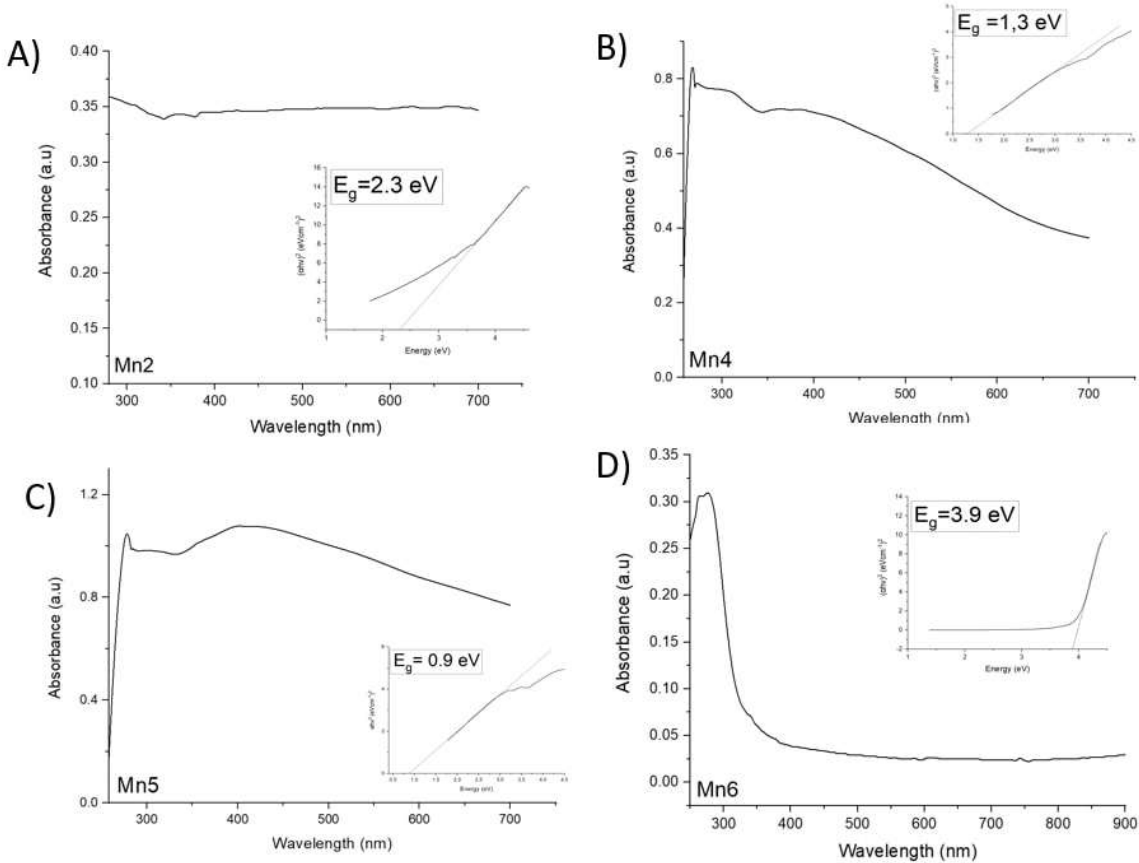


Figure 11. UV-Vis absorption spectrum of Mn-based NPs (Mn2, Mn4, Mn5, Mn6) in DMSO.

4. Conclusions

5. References

1. Altavilla, C., & Ciliberto, E. (2017). *Inorganic nanoparticles: Synthesis, applications, and perspectives*. CRC Press.
2. Toshima, N. (2004). Metal Nanoparticles for Catalysis. In: *Liz-Marzán, L.M., Kamat, P.V. (eds) Nanoscale Materials*. Springer, Boston, MA. https://doi.org/10.1007/0-306-48108-1_3
3. Wang, H., Liang, X., Wang, J., Jiao, S., & Xue, D. (2020). Multifunctional inorganic nanomaterials for energy applications. *Nanoscale*, 12(1), 14–42. <https://doi.org/10.1039/c9nr07008g>
4. Kim, T., & Hyeon, T. (2013). Applications of inorganic nanoparticles as therapeutic agents. *Nanotechnology*, 25(1), 012001. <https://doi.org/10.1088/0957-4484/25/1/012001>
5. Anselmo, A. C., & Mitragotri, S. (2015). A review of clinical translation of inorganic nanoparticles. *The AAPS Journal*, 17(5), 1041–1054. <https://doi.org/10.1208/s12248-015-9780-2>
6. Antwi-Baah, R., Wang, Y., Chen, X., Liu, H., & Yu, K. (2023). Hybrid morphologies of paramagnetic manganese-based nanoparticles as Theranostics. *Chemical Engineering Journal*, 466, 142970. <https://doi.org/10.1016/j.cej.2023.142970>
7. Haque, S., Tripathy, S., & Patra, C. R. (2021). Manganese-based advanced nanoparticles for biomedical applications: Future opportunity and challenges. *Nanoscale*, 13(39), 16405–16426. <https://doi.org/10.1039/d1nr04964j>
8. Ding, B., Zheng, P., Ma, P., & Lin, J. (2020). Manganese oxide nanomaterials: Synthesis, properties, and Theranostic Applications. *Advanced Materials*, 32(10), 1905823. <https://doi.org/10.1002/adma.201905823>
9. Keshari, A. S., & Dubey, P. (2022). Sucrose-assisted one step hydrothermal synthesis of MnCO₃/Mn₃O₄ hybrid materials for electrochemical energy storage. *Electrochimica Acta*, 402, 139486. <https://doi.org/10.1016/j.electacta.2021.139486>
10. Qian, X., Han, X., Yu, L., Xu, T., & Chen, Y. (2019). Manganese-based functional Nanoplatforms: Nanosynthetic construction, physiochemical property, and theranostic applicability. *Advanced Functional Materials*, 30(3), 1907066. <https://doi.org/10.1002/adfm.201907066>
11. Dawadi, S., Gupta, A., Khatri, M., Budhathoki, B., Lamichhane, G., & Parajuli, N. (2020). Manganese dioxide nanoparticles: Synthesis, application and challenges. *Bulletin of Materials Science*, 43(1). <https://doi.org/10.1007/s12034-020-02247-8>

12. Chen, Z., Jiao, Z., Pan, D., Li, Z., Wu, M., Shek, C.-H., Wu, C. M., & Lai, J. K. (2012). Recent advances in manganese oxide nanocrystals: Fabrication, characterization, and microstructure. *Chemical Reviews*, 112(7), 3833–3855. <https://doi.org/10.1021/cr2004508>
13. Ghosh, S. K. (2020). Diversity in the family of manganese oxides at the nanoscale: From fundamentals to applications. *ACS Omega*, 5(40), 25493–25504. <https://doi.org/10.1021/acsomega.0c03455>
14. Zhou, J., Yu, L., Sun, M., Yang, S., Ye, F., He, J., & Hao, Z. (2013). Novel synthesis of Birnessite-Type MnO₂ Nanostructure for water treatment and electrochemical capacitor. *Industrial & Engineering Chemistry Research*, 52(28), 9586–9593. <https://doi.org/10.1021/ie400577a>
15. Khatri, M., Gupta, A., Gyawali, K., Adhikari, A., Koirala, A. R., & Parajuli, N. (2022). Photocatalytic degradation of dyes using synthesized δ-MnO₂ nanostructures. *Chemical Data Collections*, 39, 100854. <https://doi.org/10.1016/j.cdc.2022.100854>
16. Ghavami, M., Soltan, J., & Chen, N. (2020). Synthesis of MnO_x/Al₂O₃ catalyst by polyol method and its application in room temperature ozonation of toluene in air. *Catalysis Letters*, 151(5), 1418–1432. <https://doi.org/10.1007/s10562-020-03393-8>
17. Ruan, J., & Qian, H. (2021). Recent development on controlled synthesis of mn-based nanostructures for bioimaging and cancer therapy. *Advanced Therapeutics*, 4(5). <https://doi.org/10.1002/adtp.202100018>
18. Sobańska, Z., Roszak, J., Kowalczyk, K., & Stępnik, M. (2021). Applications and Biological Activity of Nanoparticles of Manganese and Manganese Oxides in In Vitro and In Vivo Models. *Nanomaterials*, 11(5), 1084. <https://doi.org/https://doi.org/10.3390/nano11051084>
19. Post, J. E. (1999). Manganese oxide minerals: Crystal Structures and economic and environmental significance. *Proceedings of the National Academy of Sciences*, 96(7), 3447–3454. <https://doi.org/10.1073/pnas.96.7.3447>
20. Ghosh, S. K. (2020a). Diversity in the family of manganese oxides at the nanoscale: From fundamentals to applications. *ACS Omega*, 5(40), 25493–25504. <https://doi.org/10.1021/acsomega.0c03455>
21. Narayani, L., Jagadeesha Angadi, V., Sukhdev, A., Challa, M., Mattepanavar, S., Deepthi, P. R., Mohan Kumar, P., & Pasha, M. (2019). Mechanism of high temperature induced phase transformation and magnetic properties of Mn₃O₄ Crystallites. *Journal of Magnetism and Magnetic Materials*, 476, 268–273. <https://doi.org/10.1016/j.jmmm.2018.12.072>

22. Yang, L.-X., Zhu, Y.-J., Tong, H., Wang, W.-W., & Cheng, G.-F. (2006). Low temperature synthesis of Mn₃O₄ polyhedral nanocrystals and magnetic study. *Journal of Solid State Chemistry*, 179(4), 1225–1229. <https://doi.org/10.1016/j.jssc.2006.01.033>
23. Sicard, L., Le Meins, J.-M., Méthivier, C., Herbst, F., & Ammar, S. (2010). Polyol synthesis and magnetic study of Mn₃O₄ nanocrystals of tunable size. *Journal of Magnetism and Magnetic Materials*, 322(18), 2634–2640. <https://doi.org/10.1016/j.jmmm.2010.03.016>
24. Beknalkar, S. A., Teli, A. M., Bhat, T. S., Pawar, K. K., Patil, S. S., Harale, N. S., Shin, J. C., & Patil, P. S. (2022). Mn₃O₄ based materials for electrochemical supercapacitors: Basic principles, Charge Storage Mechanism, progress, and Perspectives. *Journal of Materials Science & Technology*, 130, 227–248. <https://doi.org/10.1016/j.jmst.2022.03.036>
25. Mohammad, F., Bwatanglang, I. B., Al-Lohedan, H. A., Shaik, J. P., Moosavi, M., Dahan, W. M., Al-Tilasi, H. H., Aldhayan, D. M., Chavali, M., & Soleiman, A. A. (2023). Magnetically controlled drug delivery and hyperthermia effects of core-shell Cu@Mn₃O₄ nanoparticles towards cancer cells in vitro. *International Journal of Biological Macromolecules*, 249, 126071. <https://doi.org/10.1016/j.ijbiomac.2023.1260>
26. Hu, Y., Wu, Y., & Wang, J. (2018). Manganese-oxide-based electrode materials for energy storage applications: How close are we to the theoretical capacitance? *Advanced Materials*, 30(47). <https://doi.org/10.1002/adma.201802569>
27. Dang, T. D., Le, T. T., Hoang, T. B., & Mai, T. T. (2015). Synthesis of nanostructured manganese oxides based materials and application for Supercapacitor. *Advances in Natural Sciences: Nanoscience and Nanotechnology*, 6(2), 025011. <https://doi.org/10.1088/2043-6262/6/2/025011>
28. Zhang, M., Chen, Y., Yang, D., & Li, J. (2020). High performance MnO₂ supercapacitor material prepared by modified electrodeposition method with different electrodeposition voltages. *Journal of Energy Storage*, 29, 101363. <https://doi.org/10.1016/j.est.2020.101363>
29. Rhadfi, T., Piquemal, J.-Y., Sicard, L., Herbst, F., Briot, E., Benedetti, M., & Atlamsani, A. (2010). Polyol-made Mn₃O₄ nanocrystals as efficient Fenton-like catalysts. *Applied Catalysis A: General*, 386(1–2), 132–139. <https://doi.org/10.1016/j.apcata.2010.07.044>
30. Mao, L., Sotomura, T., Nakatsu, K., Koshiba, N., Zhang, D., & Ohsaka, T. (2002). Electrochemical characterization of catalytic activities of manganese oxides to oxygen reduction in alkaline aqueous solution. *Journal of The Electrochemical Society*, 149(4). <https://doi.org/10.1149/1.1461378>
31. Stobbe, E. R., de Boer, B. A., & Geus, J. W. (1999). The reduction and oxidation behaviour of manganese oxides. *Catalysis Today*, 47(1–4), 161–167. [https://doi.org/10.1016/s0920-5861\(98\)00296-x](https://doi.org/10.1016/s0920-5861(98)00296-x)

32. Haque, S., Tripathy, S., & Patra, C. R. (2021). Manganese-based advanced nanoparticles for biomedical applications: Future opportunity and challenges. *Nanoscale*, 13(39), 16405–16426. <https://doi.org/10.1039/d1nr04964j>
33. Zhang, H., Xu, F., Xue, J., Chen, S., Wang, J., & Yang, Y. (2020). Enhanced removal of heavy metal ions from aqueous solution using manganese dioxide-loaded biochar: Behavior and mechanism. *Scientific Reports*, 10(1). <https://doi.org/10.1038/s41598-020-63000-z>
34. Lai, J., Wang, T., Wang, H., Shi, F., Gu, W., & Ye, L. (2018). MnO nanoparticles with unique excitation-dependent fluorescence for multicolor cellular imaging and MR imaging of brain glioma. *Microchimica Acta*, 185(4). <https://doi.org/10.1007/s00604-018-2779-5>
35. Yang, H., Zhuang, Y., Hu, H., Du, X., Zhang, C., Shi, X., Wu, H., & Yang, S. (2010). Silica-coated manganese oxide nanoparticles as a platform for targeted magnetic resonance and fluorescence imaging of cancer cells. *Advanced Functional Materials*, 20(11), 1733–1741. <https://doi.org/10.1002/adfm.200902445>
36. Zhan, Y., Zhan, W., Li, H., Xu, X., Cao, X., Zhu, S., Liang, J., & Chen, X. (2017). In vivo dual-modality fluorescence and magnetic resonance imaging-guided lymph node mapping with good biocompatibility manganese oxide nanoparticles. *Molecules*, 22(12), 2208. <https://doi.org/10.3390/molecules22122208>
37. Lin, L., Song, J., Song, L., Ke, K., Liu, Y., Zhou, Z., Shen, Z., Li, J., Yang, Z., Tang, W., Niu, G., Yang, H., & Chen, X. (2018). Simultaneous fenton-like ion delivery and glutathione depletion by MnO₂-based nanoagent to enhance chemodynamic therapy. *Angewandte Chemie International Edition*, 57(18), 4902–4906. <https://doi.org/10.1002/anie.201712027>
38. Lei, S., Peng, X., Li, X., Liang, Z., Yang, Y., Cheng, B., Xiao, Y., & Zhou, L. (2011). Novel detached system to MnCO₃ nanowires: A self-sacrificing template for homomorphous Mn₃O₄ and α -Mn₂O₃ nanostructures. *Materials Chemistry and Physics*, 125(3), 405–410. <https://doi.org/10.1016/j.matchemphys.2010.10.04>
39. Tang, Y., Chen, S., Chen, T., Guo, W., Li, Y., Mu, S., Yu, S., Zhao, Y., Wen, F., & Gao, F. (2017). Synthesis of peanut-like hierarchical manganese carbonate microcrystals via magnetically driven self-assembly for high performance asymmetric supercapacitors. *Journal of Materials Chemistry A*, 5(8), 3923–3931. <https://doi.org/10.1039/c6ta09997a>
40. Karuppaiah, M., Akilan, R., Sakthivel, P., Asaithambi, S., Shankar, R., Yuvakkumar, R., Hayakawa, Y., & Ravi, G. (2020). Synthesis of self-assembled micro/nano structured manganese carbonate for high performance, long lifespan asymmetric supercapacitors and investigation of atomic-level intercalation

- properties of OH⁻ ions via first principle calculation. *Journal of Energy Storage*, 27, 101138. <https://doi.org/10.1016/j.est.2019.101138>
41. Lee, K. K., Lee, J.-H., Lee, S. C., & Lee, C.-S. (2022). MnCO₃-mineralized polydopamine nanoparticles as an activatable theranostic agent for dual-modality imaging-guided photothermal therapy of cancers. *Theranostics*, 12(15), 6762–6778. <https://doi.org/10.7150/thno.77060>
42. Zhang, Haoyuan, Pan, X., Wu, Q., Guo, J., Wang, C., & Liu, H. (2021). Manganese carbonate nanoparticles-mediated mitochondrial dysfunction for enhanced sonodynamic therapy. *Exploration*, 1(2). <https://doi.org/10.1002/exp.20210010>
43. Cheng, Y., Zhang, S., Kang, N., Huang, J., Lv, X., Wen, K., Ye, S., Chen, Z., Zhou, X., & Ren, L. (2017). Polydopamine-coated manganese carbonate nanoparticles for amplified magnetic resonance imaging-guided photothermal therapy. *ACS Applied Materials & Interfaces*, 9(22), 19296–19306. <https://doi.org/10.1021/acsami.7b03087>
44. Ammar, S., & Fiévet, F. (2020). Polyol Synthesis: A versatile wet-chemistry route for the design and production of functional inorganic nanoparticles. *Nanomaterials*, 10(6), 1217. <https://doi.org/10.3390/nano10061217>
45. Fiévet, F., Ammar-Merah, S., Brayner, R., Chau, F., Giraud, M., Mammeri, F., Peron, J., Piquemal, J.-Y., Sicard, L., & Viau, G. (2018). The polyol process: A unique method for easy access to metal nanoparticles with tailored sizes, shapes and compositions. *Chemical Society Reviews*, 47(14), 5187–5233. <https://doi.org/10.1039/c7cs00777a>
46. Antonoglou, O., & Dendrinou-Samara, C. (2021). Polyols as a toolbox for the preparation of inorganic-based nanostructures. *Reducing Agents in Colloidal Nanoparticle Synthesis*, 51–72. <https://doi.org/10.1039/9781839163623-00051>
47. Li, J., Wu, Q., Wu, J. (2016). Synthesis of nanoparticles via solvothermal and hydrothermal methods. *Handbook of Nanoparticles*, 295–328. https://doi.org/10.1007/978-3-319-15338-4_17
48. Duan, X., Lian, J., Ma, J., Kim, T., & Zheng, W. (2010). Shape-controlled synthesis of metal carbonate nanostructure via Ionic liquid-assisted hydrothermal route: The case of manganese carbonate. *Crystal Growth & Design*, 10(10), 4449–4455. <https://doi.org/10.1021/cg1006567>
49. Pinc, J., Jankovský, O., & Bartůněk, V. (2016). Preparation of manganese oxide nanoparticles by thermal decomposition of nanostructured manganese carbonate. *Chemical Papers*, 71(6), 1031–1035. <https://doi.org/10.1007/s11696-016-0023-5>
50. Guo, H., Chen, Y., Cortie, M. B., Liu, X., Xie, Q., Wang, X., & Peng, D.-L. (2014). Shape-selective formation of monodisperse copper nanospheres and Nanocubes via disproportionation reaction route and

- their optical properties. *The Journal of Physical Chemistry C*, 118(18), 9801–9808. <https://doi.org/10.1021/jp5014187>
51. Perez De Berti, I. O., Cagnoli, M. V., Pecchi, G., Alessandrini, J. L., Stewart, S. J., Bengoa, J. F., & Marchetti, S. G. (2013). Alternative low-cost approach to the synthesis of magnetic iron oxide nanoparticles by thermal decomposition of organic precursors. *Nanotechnology*, 24(17), 175601. <https://doi.org/10.1088/0957-4484/24/17/175601>
52. Pourmortazavi, S. M., Rahimi-Nasrabadi, M., Davoudi-Dehaghani, A. A., Javidan, A., Zahedi, M. M., & Hajimirsadeghi, S. S. (2012). Statistical optimization of experimental parameters for synthesis of manganese carbonate and manganese oxide nanoparticles. *Materials Research Bulletin*, 47(4), 1045–1050. <https://doi.org/10.1016/j.materresbull.2011.12.048>
53. López-Ramón, M. V., Moreno-Castilla, C., & Fontecha-Cámarra, M. A. (2023). Removal of the oleylamine capping agent from MnFe₂O₄ hollow spheres prepared by an Ostwald ripening mechanism. *Applied Surface Science*, 612, 155796. <https://doi.org/10.1016/j.apsusc.2022.155796>
54. Cockayne, E., Levin, I., Wu, H., & Llobet, A. (2013). Magnetic structure of Bixbyite α -Mn₂O₃: A combined DFT+U and neutron diffraction study. *Physical Review B*, 87(18). <https://doi.org/10.1103/physrevb.87.184413>
55. Teng, F., Luo, S.-hua, Kang, X., Liu, Y.-guo, Shen, H.-tao, Ye, J., Chang, L.-jiao, Zhai, Y.-chun, & Dai, Y.-nian. (2019). Preparation of manganese dioxide from low-grade pyrolusite and its electrochemical performance for Supercapacitors. *Ceramics International*, 45(17), 21457–21466. <https://doi.org/10.1016/j.ceramint.2019.07.136>
56. Sakthi Kumar, D., Fujioka, M., Asano, K., Shoji, A., Jayakrishnan, A., & Yoshida, Y. (2007). Surface modification of poly(ethylene terephthalate) by plasma polymerization of poly(ethylene glycol). *Journal of Materials Science: Materials in Medicine*, 18(9), 1831–1835. <https://doi.org/10.1007/s10856-007-3033-6>